The 40 cm Monitoring Telescope of the Universitätssternwarte Bochum

M. Ramolla[1,⋆], **H. Drass**[1], **R. Lemke**[1], **C. Westhues**[1], **F. Pozo Nuñez**[1], **A. Barr Dominguez**[1], **M. Haas**[1], **R. Chini**[1,2], and **M. Murphy**[2]

[1] Astronomisches Institut, Ruhr-Universität Bochum, Universitätsstraße 150, D-44801 Bochum, Germany
[2] Instituto de Astronomía, Universidad Católica del Norte, Avenida Angamos 0610, Casilla 1280 Antofagasta, Chile

Received 2013 Feb 5, accepted 2013 May 27
Published online 2013 Dec 7

Key words quasars: emission lines – techniques: photometric – telescopes

The new 40 cm Bochum Monitoring Telescope (BMT) has started routine operation at the Universitätssternwarte Bochum (USB), located near Cerro Armazones in Chile. It has a $41' \times 27'$ field of view (FoV) and is equipped with B and V broad band filters and three narrow band filters at 670, 680, and 690 nm. This makes the BMT ideally suited to perform photometric reverberation mapping of the Hα emission line of active galactic nuclei, where the line is redshifted into the narrow bands, and to monitor bright stars which would be saturated with large telescopes. As a complement to our Robotic Bochum Twin Telescope (RoBoTT) with $2\overset{\circ}{.}7$ FoV and 14 filters, the BMT is an efficient instrument to accurately study the variability of individual sources, provided that its smaller FoV covers a sufficient number of suitable comparison stars. Here we describe the telescope and its fully robotic operation, and present science verification data demonstrating the performance of the BMT.

1 Motivation

The discovery of Mira as a prototype variable star by David Fabricius in 1596 stimulated a growing interest to search for and study the time behavior of astronomical objects – an exhausting task if done without automated techniques. Thanks to the technical feasibility of robotic instrumentation during the past decade a wealth of telescopes has been implemented or planned to monitor the night sky.

In 2009 the robotic 15 cm twin-telescope RoBoTT of the Universitätssternwarte Bochum next to Cerro Armazones in Chile has started routine operation. It has a $2\overset{\circ}{.}7$ field-of-view and is a equipped with 14 broad- and narrow band filters. RoBoTT is primarily used to investigate wide fields and for a monitoring survey of the southern galactic disk. The brightness range of $9^{\rm m} \leq R, I \leq 16^{\rm m}$, allows the photometry of stars that would be saturated with large telescopes making RoBoTT complementary to surveys like PanSTARRS or LSST (Haas et al. 2012).

By using RoBoTT we have established a novel method of photometric reverberation mapping of active galactic nuclei (AGN). Compared to well-known spectroscopic results from larger telescopes, the photometric method is an efficient tool to measure the size of the broad line region, the black hole mass and the host-galaxy subtracted AGN luminosity, even with a small telescope (Haas et al. 2011; Pozo Nuñez et al. 2012). Stimulated by this success we have commissioned the new 40 cm BMT (Fig. 1) which is ideally adapted to monitor individual objects or small fields.

⋆ Corresponding author: ramolla@astro.rub.de

Fig. 1 The BMT taking flatfield images in Summer 2012.

2 Technical properties

The telescope rests on an equatorial fork mount. Right ascension (α) and declination (δ) stepper drives have contact to the axes through friction wheels. The optical design is a Coudé system with a focal length of 2337 mm and an aperture of 413 mm. Two elliptical diagonal mirrors and a refractive Paracorr coma corrector are used. The system obscuration is 37 %.

The CCD camera is a SBIG STL-6303 with 3072×2048 9 μm pixels. The pixel scale is thus $0\overset{''}{.}79$ per pixel and the resulting field of view is approximately $41\overset{'}{.}2 \times 27\overset{'}{.}5$. The CCD is operated at -10°C, resulting in a measured gain of 1.522 e ADU^{-1} and a readout noise of 12.605 ADU.

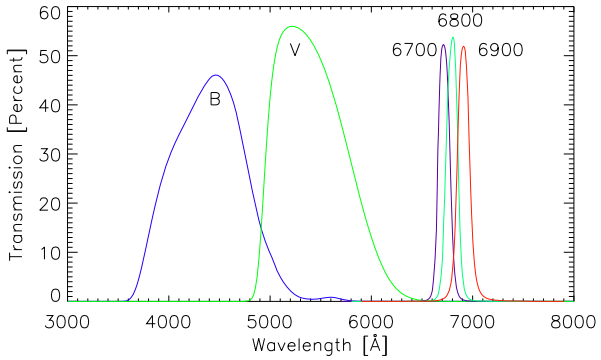

Fig. 2 Effective transmission of the filters convolved with the quantum efficiency of the Kodak 6303E CCD.

The internal filter wheel holds five slots and is currently equipped with Johnson B and V broad band filters from Astrodon and three Asahi filters with 12 nm band-pass. These are centered at 670 nm, 680 nm and 690 nm. Figure 2 shows the absolute transmission of the selected filters.

3 Observations

Observations are currently performed with predefined scripts that consist of a simple sequence of commands. The telescope control software is designed to detect critical environmental situations and respond accordingly. For example, weather conditions are read out from the observatory's weather station and promptly evaluated. If wind speed or humidity become critical, the telescope stops observations, parks and seals the tube. If conditions improve again, observations will continue; in case targets are not observable any longer, they will be replaced by the next visible alternatives. Targets will also be skipped automatically, if the moon is too close (within $10°$) to prevent too much stray light into the optical system. This is particularly important during sky-flatfield observations, when the moon may easily move too close to the observed field.

At the beginning of dusk, the telescope will move $20°$ pointed away from zenith in the east (at dawn it is $20°$ in the west). After stabilizing the detector with several readouts at the working temperature of $-10°$ C, the exposure time for flatfields will be adapted to obtain an image with a median of about 40 000 counts in all filters. If a good first exposure time is found, the control software assumes a known decrease profile of sky brightness to calculate the exposure time for the next frame. As a result, we are able to take at least 10 flatfields per night in each filter during dusk and dawn, with exposure times from 1 to 60 seconds. Note that the lower end is unproblematic because of the rolling shutter design of the camera. The flats taken under darkest sky conditions are performed in the V band and may contain thousands of stars if we observe them e.g. in the Milky Way. We reviewed the most extreme case of two consecutive nights in April 2012 (18/19), where we find two 60 s exposures (centered at $17^{\mathrm{h}}\,55^{\mathrm{m}}\,2^{\mathrm{s}}$, $-24°\,27'\,0''$ and $18^{\mathrm{h}}\,48^{\mathrm{m}}\,49^{\mathrm{s}}$, $-24°\,27'\,0''$). After dividing both masterflats, a 5×5 pixel boxcar smoothing is small enough see stellar scale artifacts together with large scale variations. Apart from about a hand full of significant bad pixels, the errors we can see compared to the expected factor of 1 across the whole image, in descending strength are

- a large scale slow variation of max 5 ‰ in the extreme corners, likely due to varying illumination of the field;
- about 30 intermediate scale relief patterns of displaced dust in the optics far off the focal plane, the maximum variation among all these features is 2 ‰;
- about a hand full of very weak stellar scale artifacts, the strongest deviation is 2 ‰.

Concluding, the flatfields are reliable within the above mentioned precision. In case of doubts, all calibration images are archived and can be reviewed in comparison to the reduced frames and calibration data from adjacent nights. The flatfields are not multiplied by a field illumination map. A varying photometric zero point is corrected after photometry, by calculating a map of photometric offsets for a calibration field that has been observed with the same filter.

The flatfield- and dark corrected image may contain cosmic rays, hot pixels, flatfield-errors and damaged columns or rows. These problems have to be accounted for before a reliable photometry is possible. Dithering around the selected target position poses a useful solution to this. We employed a dithering algorithm in the control software. The purpose is to maximize resolution enhancement potential by over-sampling and to reliably eliminate detector errors and cosmic ray hits. The dithering will be executed along a predefined 9-point-square pattern. Each point has a distance of 26.88 pixels to its next neighbors. On one hand, this size is chosen to avoid small scale detector errors and cosmic ray events, but on the other hand also to avoid large information loss at the borders or mixing different stray-light gradients in the field of view. The pattern is rotated about $18.^{\circ}42$ from the α detector axis. Hence, the projection of the pattern along the α and δ axis has equidistant sampling with $\approx$8.5 pixel distance, thus ruling out all column and row errors being smaller than this.

Each second image is shifted $n + 0.5$ pixels relative to the last one and we will refer to this principle as half-pixel shifts. These relative shifts are chosen to improve the resolution in the resampling process. Due to the astrometric matching of at least hundreds of sources in each single image, it is possible to reconstruct the sub-pixel shifts between the images. After an astrometric solution is found, images will be resampled onto a world coordinate grid with $2\times$ the original resolution. However, the physical resolution in the images will be primarily dependent on observing parameters, like wind, seeing or a good tracking during the exposure. The resolution gain of the resampling will naturally be the higher, the more the PSF on the source frames is undersampled.

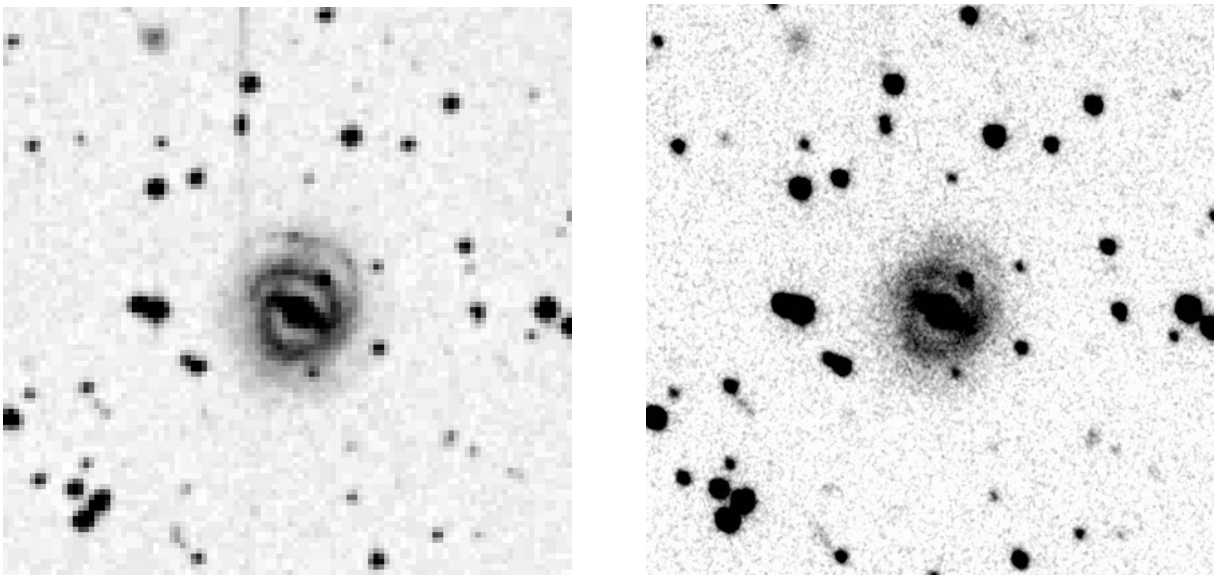

Fig. 3 Comparison between V band images from the POSS1 survey (*left*) and our 40 cm for ESO 374-G25 (*right*). The effective aperture of the Palomar Schmidt telescope is 1.26 m – three times larger than that of the BMT. Both images span $5' \times 5'$, with North being up and East to the left.

The pointing model is described through Eqs. (1) and (2) below. IH and ID are the encoder index offsets. NP accounts for the misalignment between δ and hour angle h. CH is the term for the misalignment between the polar axis and declination axis (collimation error in east-west direction). ME is the coefficient for vertical misalignment of the polar axis. MA represents the azimuthal misalignment of the polar axis. TF represents the tube flexure and FO the fork flexure. A_1 and A_2 are additional terms, chosen to leverage slowly varying residual errors across the sky.

$$\begin{aligned}\Delta h = {} & \mathrm{IH} + \mathrm{NP}\tan\delta + \mathrm{ME}\sin h\tan\delta \\ & + \mathrm{CH}\sec\delta - \mathrm{MA}\cos h\tan\delta \\ & + \mathrm{TF}\cos\phi\sin h\sec\delta + \mathrm{A}_1\sin h\cos\delta,\end{aligned} \tag{1}$$

$$\begin{aligned}\Delta\delta = {} & \mathrm{ID} + \mathrm{ME}\cos h + \mathrm{MA}\sin h \\ & + \mathrm{TF}\left(\cos\phi\cos h\sin\delta - \sin\phi\cos\delta\right) \\ & + \mathrm{FO}\cos h + \mathrm{A}_2\tan\delta\end{aligned} \tag{2}$$

The coefficients of our model are calculated from the offsets of 400 random pointings that were generated over the entire visible sky above 40° elevation (our lower observability boundary). The recorded images were matched against the USNO-B1 catalog.

The resulting pointing model is accurate within about $5'$. Our precision suffers still from randomly appearing offsets which are mostly related to slipping in the mechanics and are dependent on the previous movement paths of the mount. To account for this uncertainty, the script control software of the telescope matches images taken during focussing (performed before starting observations of every different field) to the astrometric catalog mentioned before. The α and δ offsets gained from this are then used to reposition the telescope before taking science images, now precise within $10''$ on the undithered pointing.

4 Data reduction

The data are transferred to Bochum via the EVALSO network[1], where they are reduced in a standard manner by automatic scripts. The steps can be summarized as follows:

- For each night and filter, 20 bias, 20 dark and 10 flatfield images (from the beginning and end of the observations) are used for standard manner IRAF reduction of the raw data.
- Then, SOURCEEXTRACTOR[2] is used to extract a catalog of positions of sources, in order to match them with the USNO-B1 astrometric reference catalog.
- This is performed using SCAMP[3], which also determines image projection and distortion parameters. If these cannot be determined satisfactorily, median values are used instead. These median values have been determined from analyzing a set of images with reliable astrometric matching on the full frame.
- Provided the image offsets and distortion correction, we can now apply SWARP[4]. Using this tool, the images are then resampled to a new grid with a pixel size of $0\farcs39 \times 0\farcs39$ that is perfectly aligned to the ordinates of the world coordinate system.
- Using the IRAF task "imcombine", the image-sets are then combined with min/max rejection, to eliminate dead pixels, or cosmic ray events. Compared to pure median combination, this average yields a better signal-to-noise ratio. The products of this pipeline are trimmed combined images with about 5500×3500 pixel size.

[1] Enabling Virtual Access to Latin-America Southern Observatories
[2] http://www.astromatic.net/software/sextractor
[3] http://www.astromatic.net/software/scamp
[4] http://www.astromatic.net/software/swarp

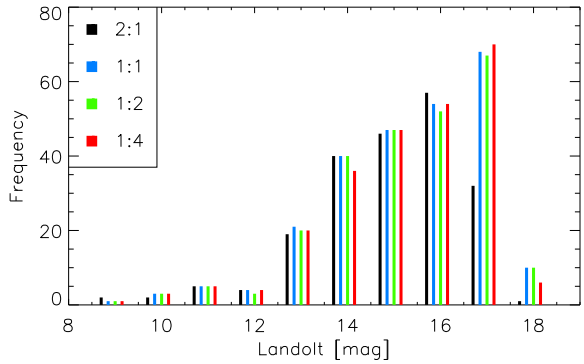

Fig. 4 Photometric completeness of the Landolt field SA 95 per apparent magnitude. Colors distinguish the different resampling resolutions used in the data reduction. Black is artificial undersampling to $1\farcs58$ pixels (2:1). For blue, the original pixel size is kept (1:1). Green is with $2\times$ oversampling to $0\farcs39$ pixels (1:2), while red shows the result for $4\times$ oversampling (1:4).

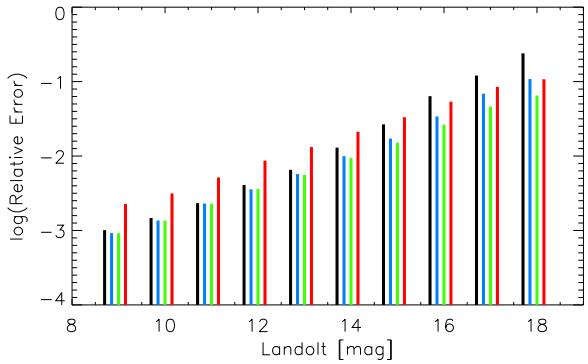

Fig. 5 Relative photometric errors of the Landolt field SA 95 per apparent magnitude for different resampling rates. The colors are identical to those in Fig. 4. Photometry was performed with an $7\farcs9$ fixed aperture.

5 Image quality

Figure 3 shows images of the Seyfert-1 galaxy ESO 374-G25 and its surrounding stars. Both contrast and spatial resolution reach at least the quality of a Digitized Sky Survey (DSS) image of the Palomar Schmidt telescope with an 1.26 m effective aperture. Stellar profiles in the right-hand image have a lower effective resolution ($3\farcs2$ FWHM of point sources, compared to $2\farcs9$).

We have performed photometric tests on the standard star field SA 95 (Landolt 2009). Five dithered exposures over 30 seconds in the broad- and 60 seconds in the narrow bands have been taken, respectively. Since the photometric properties in all filters are essentially the same, we focus on the V band images, which are the deepest in this set.

Now we will explain why the data is resampled onto a grid with half the pixel size of the original data. There are no huge gains to be expected, because stars on the input images are not undersampled, if we compare their FWHM of $\sim 3\farcs1$ to the pixel size of $0\farcs79$. But to investigate differences, we modify our reduction pipeline to resample the data to coordinate grids of which the resolution scales by the power of two different from the original data. Intermediate scales are not considered because of the potential influence of the Moiré-effect.

Figure 4 shows that an additional undersampling of the data to large $1\farcs58$ pixels will destroy information, which can be seen in the missing weaker objects $\gtrsim 17^{\rm m}$. All other resolutions yield effectively the same detection rates. If we plot the average relative photometric errors in an $7\farcs9$ fixed aperture (diameter) photometry by SourceExtractor for each magnitude bin, as in Fig. 5, we see that there are only minimal differences, but overall, and especially for weaker sources, the $2\times$ resampling yields the lowest relative errors.

Moreover, because of our dithering strategy in the observations, with shifts of multiples of 1/2 pixel size along the detector axes, we will also have a slight gain in spatial information by the resampling. This can be roughly evaluated by considering the average FWHM size falling from $3\farcs2$ on the original data to $3\farcs1$ on the $2\times$ resampled image. Considering this, we can conclude that the $2\times$ resampling of our data has a positive effect even on simple aperture photometry. Concluding, the gains in the data quality justify quadrupling the amount of data to be stored.[5]

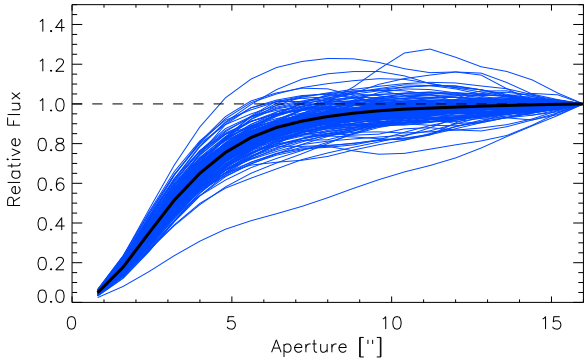

Fig. 6 Flux dependence on aperture size in the V band, determined from 200 isolated stars in the Landolt standard star fields. The thick black line is the mean of individual stars shown by the colored dotted lines. The results for V are indistinguishable from all other bands.

After standard reduction in our pipeline, we applied aperture photometry for 20 apertures ranging equidistantly from $0\farcs8$ to $16\farcs0$. Figure 6 shows the curve of growth of the V band fluxes for 200 isolated stars in the Landolt field. The thick black line follows the median, showing that the current optical system delivers an average point-spread function with about $3\farcs1$ full width at half maximum.

With the errors associated to our aperture photometry, we can calculate an optimal aperture for each of the stars in this V band image. We consider this aperture to be the minimum of the noise-per-signal function of each object.

[5] Currently $\sim$80 Megabyte per reduced image.

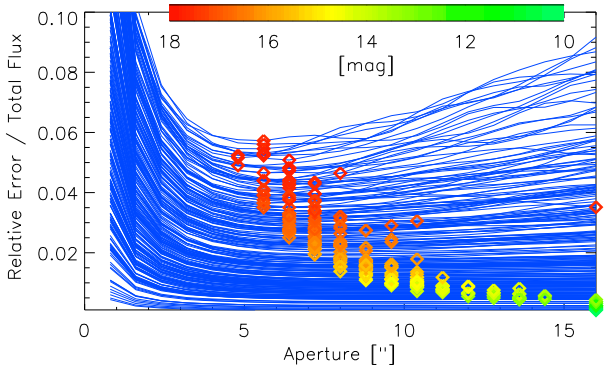

Fig. 7 Relative error per measured total flux as a function of the apertures. Each blue line represents an individual isolated star from the Landolt field. The colored diamonds represent the minima of the respective relative error curves.

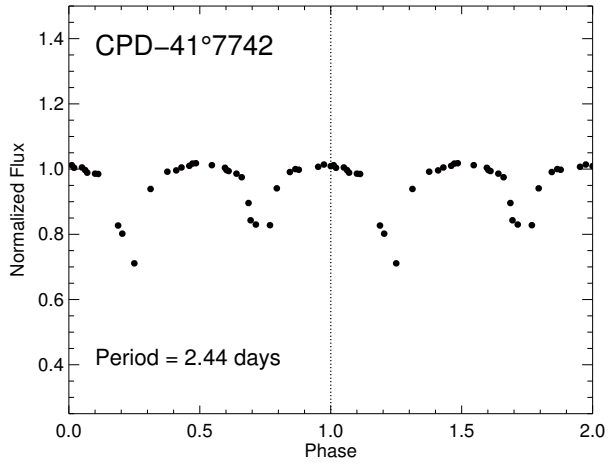

Fig. 8 Phase diagram of the O-star CPD –41°7742. The photometric errors are of the order of the symbol sizes. The derived period of 2.44 days and the two different minima agree with literature values.

Figure 7 shows these curves together with the minima represented by rainbow-colored diamonds. The colors are associated to the apparent magnitudes of the objects, which have been cross-calibrated with the Landolt standards in the field. As expected, the weak sources have a higher overall noise and the optimal apertures are smaller. With our 5×30 second exposure, we can reach $17^{\rm m}$ as a 2σ detection with an optimum aperture of $6''$. For stars brighter $10^{\rm m}$, the optimum appears to lie even above $16''$, but as these sources are close to saturation this has to be treated with caution.

6 Light curves

Until January 2013, a dozen AGN and 42 variable young stars have been monitored with the BMT. We here illustrate the results of two examples: i) the lightcurve of the bright eclipsing binary CPD –41°7742 with known orbit parameters and ii) the reverberation mapping of the Seyfert-1 galaxy RX J1741.4+0348.

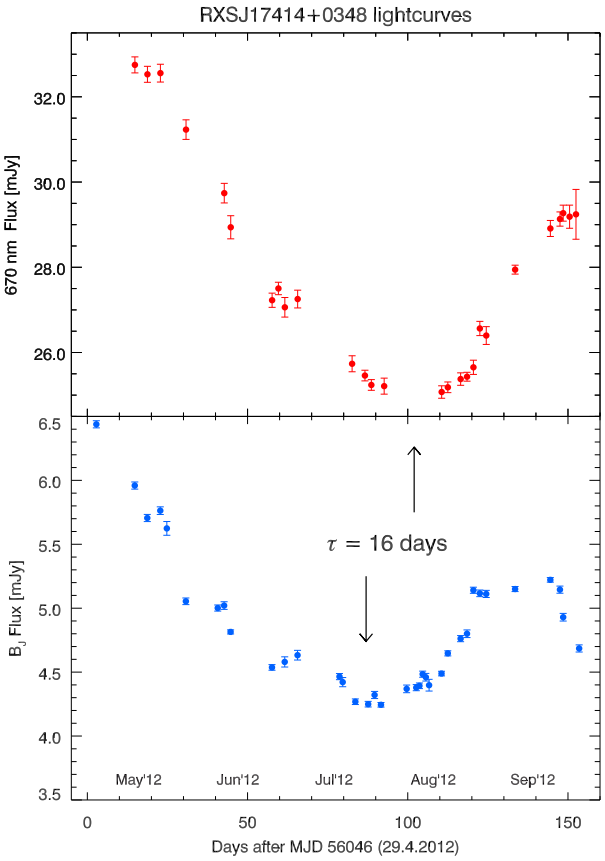

Fig. 9 Light curves of RX J1741.4+0348 in the B band (blue) and 670 nm NB (red). The minimum of the NB light curve lags that of the B band by about τ = 16 d.

Figure 8 shows the phase curve of the $V \sim 8.2^{\rm m}$ eclipsing binary CPD –41°7742. The 670 nm light curve with 32 data points was obtained during 2 months of observations in summer 2012. Using the Lafler-Kinman algorithm (Lafler & Kinman 1965) which is best suited for period finding of low-number light curves (e.g. Haas et al. 2012). We obtain a period of 2.44 ± 0.02 d which agrees well with the result ($P = 2.44069 \pm 0.00043$ d) determined by Sana et al. (2003). Also the depth of the two minima is consistent with the values ($\sim$0.7 and $\sim$0.8) found by Sana et al. (2003).

AGN light curves are taken over several months with a time sampling of 1 to 3 days, depending on the intrinsic luminosity of the nucleus, which determines the size of the BLR and thus allows to predict the time lag of the echo. Figure 9 shows light curves in broad and narrow bands of the Seyfert-1 galaxy RX J1741.4+0348. At a redshift of $z = 0.30$ the Hα emission line shifts to 676 nm, hence into the 670 nm and 680 nm NBs. The good quality of the curves allows us to see the time delay of the 670 nm NB (most likely dominated by the Hα line) to the B band continuum variation by eye to be about 16 days (marked by the black arrows in Fig. 9). A detailed study of the light curves of RX J1741.4+0348, together with other AGN, will be presented in a forthcoming publication.

7 Summary and outlook

We presented the concept and first results of the new robotic 40 cm monitoring telescope of the USB. The current status of the project can be summarized as follows:

- Observing is performed by autonomous software, controlling all telescope hardware components. Frames are dithered in a fixed pattern, primarily to eliminate detector errors, but also cosmic ray events and increase the spatial information by subpixel shifts.
- Data are transferred in Bochum and reduced by an automatic reduction pipeline. After applying standard calibration, images are matched with astrometric reference catalogs (USNO-B1). The frames are then averaged with min/max-rejection to a combined image.
- Observing 5×30 seconds in V band results in 2σ detections of 17^{m} stars. The optimal fixed aperture for photometry in this case is then $6''$.

For the intended purpose of variability studies of bright stars and AGN narrow band reverberation mapping, our setup already delivers excellent results, demonstrating the performance of the BMT. In the near future, the BMT will open the possibility to accurately monitor dozens of bright stars or up to 10 AGN with $V \lesssim 15.5^{\mathrm{m}}$ per night.

Acknowledgements. This project is supported by the Nordrhein-Westfälische Akademie der Wissenschaften und der Künste in the framework of the academy program by the Federal Republic of Germany and the state Nordrhein-Westfalen. This work has made use of the NASA/IPAC Extragalactic Database (NED) which is operated by the Jet Propulsion Laboratory, California Institute of Technology, under contract with the National Aeronautics and Space Administration. We thank Bo Reipurth for his efforts in the early phases of this project, and for providing the main mirror and other optical elements. We thank our referee for valuable comments that helped to clarify the manuscript. This work is supported by the DFG Program (HA 3555/12-1). The observations on Cerro Armazones benefited from the care of the guardians Hector Labra, Gerardo Pino, Roberto Munoz, and Francisco Arraya.

References

Haas, M., Chini, R., Ramolla, M., et al. 2011, A&A, 535, A73
Haas, M., Hackstein, M., Ramolla, M., et al. 2012, Astron. Nachr., 333, 706
Lafler, J., & Kinman, T. D. 1965, ApJS, 11, 216
Landolt, A. U. 2009, AJ, 137, 4186
Pozo Nuñez, F., Ramolla, M., Westhues, C., et al. 2012, A&A, 545, A84
Sana, H., Hensberge, H., Rauw, G., & Gosset, E. 2003, A&A, 405, 1063

